



UNIVERSITY OF LEEDS

This is a repository copy of *Integrated hydro-mechanical and seismic modelling of the Valhall reservoir: A case study of predicting subsidence, AVOA and microseismicity*.

White Rose Research Online URL for this paper:
<http://eprints.whiterose.ac.uk/86240/>

Version: Accepted Version

Article:

Angus, DAC, Dutko, M, Kristiansen, TG et al. (7 more authors) (2015) Integrated hydro-mechanical and seismic modelling of the Valhall reservoir: A case study of predicting subsidence, AVOA and microseismicity. *Geomechanics for Energy and the Environment*, 2. pp. 32-44. ISSN 2352-3808

<https://doi.org/10.1016/j.gete.2015.05.002>

© 2015, Elsevier. Licensed under the Creative Commons Attribution-NonCommercial-NoDerivatives 4.0 International
<http://creativecommons.org/licenses/by-nc-nd/4.0/>

Reuse

Unless indicated otherwise, fulltext items are protected by copyright with all rights reserved. The copyright exception in section 29 of the Copyright, Designs and Patents Act 1988 allows the making of a single copy solely for the purpose of non-commercial research or private study within the limits of fair dealing. The publisher or other rights-holder may allow further reproduction and re-use of this version - refer to the White Rose Research Online record for this item. Where records identify the publisher as the copyright holder, users can verify any specific terms of use on the publisher's website.

Takedown

If you consider content in White Rose Research Online to be in breach of UK law, please notify us by emailing eprints@whiterose.ac.uk including the URL of the record and the reason for the withdrawal request.



eprints@whiterose.ac.uk
<https://eprints.whiterose.ac.uk/>

1 **Integrated hydro-mechanical and seismic modelling of the Valhall reservoir: A**
2 **case study of predicting subsidence, AVOA and microseismicity**

3
4 D.A. Angus¹, M. Dutko², T.G. Kristiansen³, Q.J. Fisher¹, J-M. Kendall⁴, A.F. Baird⁴, J.P. Verdon⁴, O.I.
5 Barkved^{3,5}, J. Yu² and S. Zhao²

6
7 ¹ University of Leeds, Leeds, UK

8 ² Rockfield Software Ltd, Swansea, UK

9 ³ BP, Stavanger, Norway

10 ⁴ University of Bristol, Bristol, UK

11 ⁵ Current address, Petoro AS, Øvre Strandgate 124, 4002 Stavanger, Norway

12
13
14 **Abstract:**

15 Geomechanical, fluid-flow and seismic modelling have been combined to predict surface
16 subsidence, seismic anisotropy and microseismicity for the Valhall reservoir, North Sea. The
17 constitutive model used in the geomechanical simulation consists primarily of layers having
18 poro-elastic behaviour, but with poro-elasto-plasticity behaviour in the chalk reservoir units.
19 The constitutive model incorporates matrix deformation during simulation, such that areas of
20 compaction and dilation are modelled so that the likely microseismic response of the
21 reservoir can be predicted. In the coupled fluid-flow and geomechanical (hydro-mechanical)
22 workflow, a finite-element geomechanical simulator is coupled to a reservoir fluid-flow
23 simulator and applied to predict seafloor subsidence. Subsequently, the history-matched
24 hydro-mechanical results are transformed into dynamic elastic models suitable for seismic
25 analysis using an empirical static-to-dynamic relationship and stress-dependent rock physics
26 model. The elastic models are then used to predict seismic anisotropy and microseismicity,
27 allowing for an additional assessment of hydro-mechanical simulation via comparison with
28 observed field seismic data. The geomechanical model has been calibrated to reproduce the
29 measured subsidence. Furthermore, the predicted seismic anisotropy extracted from the
30 reflection amplitude variation with offset and azimuth resembles that measured from field
31 seismic data, despite the limited calibration of the rock physics model to the Valhall reservoir
32 rocks. The spatial pattern of modelled microseismicity is consistent with previously published
33 microseismic analyses, where the modelled failure mechanisms are consistent with typical
34 production-induced seismicity. The results of this study indicate that seismic data has the
35 potential to improve the calibration of hydro-mechanical models beyond what is possible from

36 conventional fluid production and surface subsidence data. This is significant as seismic data
37 could provide greater control over the whole field rather than borehole and surface
38 measurements.

39 **1. Introduction**

40 Extraction and injection of fluids within petroleum reservoirs alters the ambient pore pressure
41 leading to changes in the effective stress field within the reservoir and surrounding rocks.
42 From the perspective of seismic monitoring, changes in the stress field can lead to nonlinear
43 changes in seismic velocity observable in time-lapse seismic data (e.g., Barkved et al. 2003;
44 Herwanger & Horne 2005; Barkved & Kristiansen 2005; Kristiansen et al. 2005). However,
45 changes in pore pressure do not necessarily lead to a hydrostatic change in effective stress.
46 For instance, a reduction in fluid pressure within a reservoir is often accompanied by a
47 slower increase of the minimum effective horizontal stress with respect to the vertical
48 effective stress change (e.g., Hillis 2001). This asymmetry can result in the development of
49 stress anisotropy that may promote failure within the rock, such as fault reactivation and
50 casing deformation. This has important implications on the interpretation of time-lapse
51 seismic as well as microseismic data, where stress anisotropy can result in anisotropic
52 perturbations in the velocity field (e.g., Herwanger & Horne 2009) leading to induced seismic
53 anisotropy, offset and azimuthal variations in reflection amplitudes, shear-wave splitting, and
54 microseismicity if the stress exceeds the strength of the rock mass.

55 Over the past several decades, significant advances have been made in monitoring and
56 predicting changes in physical properties within the subsurface related to petroleum
57 production (e.g., Calvert 2005; Fjær & Kristiansen 2009; Johnson 2013). Yet uniquely
58 relating surface deformation and time-lapse seismic observations to changes in rock physical
59 properties is challenging (e.g., Herwanger et al. 2010). Recent improvements in the
60 integration of coupled fluid-flow and geomechanical (or hydro-mechanical) simulation with
61 rock physics and seismic modelling have led to a better understanding of changes in the
62 physical properties of the subsurface and their time-lapse seismic signature (e.g., Olden et

63 al. 2001; Minkoff et al. 2004; Herwanger & Horne 2005, 2009; Angus et al. 2011, Trudeng et
64 al. 2014, He et al. 2015). Time-lapse seismic attributes have non-unique interpretations; for
65 instance, observed changes could be due to changes in fluid saturation or to changes in the
66 rock fabric itself (e.g., compaction). Hydro-mechanical modelling combined with seismic
67 measurement and interpretation have the potential to help distinguish between these effects,
68 and hence improve drilling (Kristiansen & Flatebø 2009) and completion practices, and
69 identify areas where more production can be achieved. If successful, this would help reduce
70 both the costs of conventional and unconventional production by reducing the number of
71 wells necessary to achieve production targets.

72 In this paper, we integrate geomechanical, fluid-flow and seismic modeling to simulate the
73 stress evolution during production to predict surface deformation and seismic attributes. A
74 finite-element geomechanical simulator (ELFEN) is coupled to a reservoir fluid production
75 simulator (VIP), where the output from the hydro-mechanical simulation is used to model
76 surface subsidence, the seismic attribute AVOA (reflection amplitude versus offset and
77 azimuth), and reservoir and overburden microseismicity. The integrated hydro-mechanical
78 and seismic modelling workflow is applied to the data-rich Valhall oil reservoir in the southern
79 part of the Norwegian sector of the North Sea. The field produces from relatively weak chalk
80 in the Tor and Hod formations of Late Cretaceous age at a depth of about 2400 meters. The
81 field likely began deforming elastically, but over time transitioned to plastic deformation in
82 some regions in the form of reservoir compaction, and this accelerated due to water
83 weakening from pressure support. Hence Valhall has presented numerous geomechanical
84 difficulties during its production lifespan. We compared predicted subsidence, AVOA
85 response and microseismicity with observations from field data.

86 **2. Hydro-mechanical and seismic modelling**

87 Recent studies linking numerical coupled fluid-flow and geomechanical simulation with
88 seismic modelling have improved our understanding of the relationship between seismic
89 attributes, fluid properties and mechanical deformation due to reservoir fluid extraction and

90 injection (e.g., Rutqvist et al. 2002; Dean et al. 2003; Herwanger & Horne 2009; Alassi et al.
91 2010; Angus et al. 2010; Herwanger et al. 2010; Schoenball et al. 2010; Verdon et al. 2011).
92 Analytic and semi-analytic approaches using poroelastic formulations for simple geometries
93 have been used previously to understand surface subsidence (e.g., Geertsma 1973),
94 microseismicity (e.g., Segall 1989) and seismic travel-time shifts (e.g., Fjær & Kristiansen
95 2009; Fuck & Tsvankin 2009; Fuck et al. 2011) due to pore pressure changes. Within the
96 past decade, there has been significant effort to develop coupled fluid-flow and
97 geomechanical numerical simulators primarily because they can be applied to more realistic
98 geometries (e.g., Rutqvist et al. 2002; Dean et al. 2003; Minkoff et al. 2003; Herwanger &
99 Horne 2009; Segura et al. 2011). Numerical hydro-mechanical simulators can integrate the
100 influence of multi-phase fluid-flow as well as deviatoric stress and strain to provide more
101 accurate models of the spatial and temporal behaviour of various rock properties within and
102 outside the reservoir (e.g., Herwanger et al. 2010). Linking changes in reservoir physical
103 properties, such as porosity, permeability and bulk modulus, to changes in seismic attributes
104 is accomplished via rock physics models (e.g., Prioul et al. 2004) to generate so-called
105 dynamic (high strain rate and low strain magnitude suitable for seismic frequencies) elastic
106 models.

107 **2.1 Hydro-mechanical modelling**

108 **Coupling method:** Industry standard fluid-flow simulators solve the equations of flow for
109 multi-phase fluids (e.g., Aziz & Settari 1979), but tend to neglect the influence of changing
110 pore pressure on the geomechanical behaviour of the reservoir and surrounding rock, when
111 processes such as stress arching are active (Minkoff et al. 2003; Segura et al. 2011). There
112 are a considerable number of published papers related to the importance and applicability of
113 coupled reservoir fluid-flow and geomechanical modelling. For example, Gutierrez & Lewis
114 (1998) show that compaction drive is not only dependent on the compressibility of the
115 reservoir, but also the downward movement of the overburden, which cannot be properly
116 accounted for without performing a coupled simulation. Dean et al. (2003) show that the

117 merit of explicit or coupled simulation is dependent on reservoir compaction scenario and the
118 compressibility of the pay and non-pay formations. Formulations exist for fully coupled fluid-
119 flow and geomechanical simulation, yet they tend to be computationally expensive (e.g.,
120 Minkoff et al. 2003) and often limited to single-phase flow. Iterative and loosely coupling fluid-
121 flow simulators with geomechanical simulators can be computationally more efficient, yet
122 yield sufficiently accurate results compared to fully coupled solutions (e.g., Dean et al. 2003;
123 Minkoff et al. 2003). Furthermore, iterative and loosely coupled approaches allow the use of
124 already existing commercial reservoir fluid-flow and geomechanical modelling software. The
125 coupling scheme employed in this paper is a staggered (incremental) external coupling
126 method (see Figure 1).

127 [Figure 1 here]

128 **Constitutive model:** Predicting the geomechanical response of reservoirs depends on the
129 ability of the geomechanical simulator to model the nonlinear behaviour of rocks. The
130 nonlinear dependence of rocks with stress is generally attributed to the deformation of
131 microcracks and pores, grain-boundary contacts, and fractures with changing confining
132 stress (e.g., Rutqvist 1995; Herwanger & Horne 2009). Rock properties also display stress
133 hysteresis (e.g., Helbig & Rasolofosaon 2000; Hueckel et al. 2001; Ferronato et al. 2013)
134 and this hysteresis has been observed to occur not only at large strains but also small strains
135 (Johnson & Rasolofosaon 1996). Hysteresis represents a potentially important rock
136 characteristic in explaining the asymmetric behaviour of 4D seismic observations of
137 producing reservoirs (Hatchell & Bourne 2005). In this paper, the constitutive relationship
138 used by the geomechanical simulator is the so-called SR3 (Soft Rock 3) model (see
139 Appendix A1) and is derived from laboratory experiments that incorporate linear poro-elastic
140 and poro-plastic behaviour (e.g., Crook et al., 2002) as well as lithology specific deformation
141 (e.g., Crook et al., 2006), where the model can be applied to various rock types such as
142 sandstone, shale and chalk. For more details on coupling procedures between the
143 geomechanical simulator and reservoir simulator see Angus et al. (2011) and Segura et al.

144 (2011). An analysis of when coupling is needed is provided in Segura et al. (2011). An
145 additional feature of the SR3 model used for the Valhall simulation was the addition of chalk
146 water weakening, where the yield surface properties are dependent on the change in water
147 saturation compared to a reference state.

148 **2.2 Integrated seismic modelling**

149 **Rock physics model:** To model the seismic response due to geomechanical deformation,
150 rock physics models are required to link changes in fluid saturation, pore pressure and
151 triaxial stresses to changes in the dynamic elastic stiffness. These models should incorporate
152 phenomena observed in both laboratory core experiments and in the field, such as the non-
153 linear stress-velocity response (e.g., Nur & Simmons 1969; Sayers 2007; Hatchell & Bourne
154 2005) and the development of stress-induced anisotropy in initially isotropic rocks (Dewhurst
155 & Siggins 2006; Olofsson et al. 2003; Fjær & Kristiansen 2009). The nonlinear rock physics
156 model is generally incorporated within an aggregate elastic model (see Angus et al. 2011).
157 The approach has the benefit of allowing us to incorporate phenomena that act on multiple
158 length-scales. Intrinsic anisotropy, caused by alignment of anisotropic minerals (such as
159 clays and micas), can be included using an anisotropic background elasticity that can be
160 constrained by laboratory methods (e.g., Valcke et al. 2005; Kendall et al. 2007). Stress-
161 induced seismic anisotropy, due to anisotropic changes in the effective stress field, is
162 incorporated implicitly within the non-linear rock physics model. In other words, where there
163 is a larger change in effective stress in one direction compared to another, the behaviour of
164 the microcracks will vary in these directions leading to anisotropic changes in seismic
165 velocity. Finally the influence of larger-scale sub-seismic fracture sets can also be modelled
166 using the Schoenberg & Sayers (1995) effective medium approach, adding the additional
167 compliance of the larger fracture sets to the stress-sensitive compliance. Fluid substitution
168 can also be included using either the Brown & Korringa (1975) anisotropic extension to
169 Gassmann's equation, which is appropriate as a low-frequency end member, or incorporating
170 the dispersive effects of squirt-flow between pores (Chapman, 2003).

171 In this paper, we focus solely on the effects of nonlinear stress dependence of seismic
172 velocities and assume that the rock has no intrinsic anisotropy or effective anisotropy due to
173 the presence of coherent large-scale fracture sets. This is an entirely reasonable assumption
174 given the weak nature of the reservoir and overburden. Several approaches have been
175 developed to account for the influence of changes in stress and development of strain on
176 seismic velocities, such as the one-dimensional vertical strain model (Hatchell & Bourne
177 2005), the third-order elasticity theory model (Prioul et al. 2004; Herwanger & Horne 2009),
178 and the microcrack excess compliance model (Sayers 2007; Hall et al. 2008; Verdon et al.
179 2008). Angus et al. (2009; 2012) use ultrasonic core data to calibrate the microcrack model
180 of Verdon et al. (2008) and observe that the rock physics input parameters have relatively
181 consistent values that are specific to lithology (see Appendix A2). Estimates of microcrack
182 initial aspect ratio for most lithologies have mean of 0.0005, but differ for shale by up to an
183 order of magnitude with mean of 0.001. Estimates of initial crack density are more diffuse,
184 and are believed to be sensitive to core damage, microcrack/grain-boundary geometry and
185 diagenesis. Based on the results of the calibration studies (Angus et al., 2009; 2012), we use
186 the scalar microcrack analytic model as it yields a reasonably accurate prediction of the
187 nonlinear stress dependence of seismic velocities and anisotropy. Table 1 shows the layer
188 specific values used for the model initial crack density and initial aspect ratio.

189 **AVOA prediction:** In AVOA analysis, multi-offset and multi-azimuth reflection amplitude
190 data are reduced to a set of parameters, such as the normal incidence amplitude and the
191 principal AVO gradients. Generally only short-offset data are considered, where the variation
192 in reflection amplitudes with azimuth (ϕ) can be described by a simple $\cos^2\phi$ trend (e.g.,
193 Ruger 1998). Hall & Kendall (2003) calculate AVOA parameters in three key stages. First, a
194 three-term AVO curve is calculated using data in overlapping 25 m x 25 m common midpoint
195 bins. Second, the normal-incidence amplitude term is used to evaluate the azimuthal
196 dependent near-offset AVO gradient term. Finally, the AVOA algorithm assumes the near-
197 offset AVO gradient is elliptical allowing the orientation and magnitude of anisotropy to be

198 determined from the AVO coefficients. Although the AVOA observations of Hall & Kendall
199 (2003) are a measure of the near-offset AVO gradient and not velocity anisotropy, the
200 method provides a measure of fracture orientation and strength. Velocity anisotropy can be
201 estimated using an effective fractured medium rock physics model (e.g., Hall, 2000).

202 To predict the AVOA response, we calculate the complex valued reflection coefficients using
203 an anisotropic layer-matrix approach (e.g., see Angus & Thomson 2012 for description of the
204 theory). The reflection coefficient of any interface between two layers is evaluated using the
205 elasticity tensor of the upper and lower layer. For the Valhall model, the algorithm provides
206 synthetic amplitudes at specified offsets and azimuths for each grid point within the hydro-
207 mechanical seismic sub-volume and for each chosen horizon. The predicted AVOA response
208 will be sensitive to the geometry of the model as well as the stress-dependence of the
209 nonlinear microcrack rock physics transform (see Appendix B).

210 **Microseismic model:** An important observable manifestation of geomechanical deformation
211 is brittle failure, which can be linked to microseismic activity. Regions that have high shear
212 stress have an increased risk of brittle failure, implying higher microseismicity rates. If
213 mechanical simulations include brittle and plastic behaviour in their constitutive models, then
214 regions of high shear stress or matrix failure can be used as direct indicators of microseismic
215 activity. There remains a degree of uncertainty regarding the best method of predicting
216 microseismic activity based on finite-element geomechanical models.

217 We have developed two parallel methods to predict microseismicity on reservoir field scale
218 using finite-element hydro-mechanical simulations. The first approach is applied to
219 poroelastic simulations and considers the evolution of deviatoric stress with respect to the
220 Mohr-Coulomb failure envelope. This can be formalized using the fracture potential term
221 (e.g., Verdon et al. 2011), which describes the ratio of the in-situ deviatoric stress to the
222 critical stress required for failure on an optimally oriented surface. A higher value for fracture
223 potential corresponds to a higher risk of microseismicity for the node in question. The second
224 approach is applied to poroelastoplastic simulations and involves tracking matrix failure

225 during the geomechanical simulation (Angus et al. 2010). This microseismic modeling
226 method allows for a continuous prediction of the temporal and spatial distribution of
227 seismicity. In this approach, the geomechanical simulator internally tracks regions
228 undergoing yield and for each failure event, the stress tensor, pore pressure and elastic
229 tensor are recorded. In this study, the matrix failure approach to microseismic prediction is
230 used to provide an estimate (i) of regions within the model that might generate seismicity,
231 and (ii) direction and type of the failure (tensile, shear or shear-enhanced compaction).

232 **3. Valhall model**

233 The Valhall reservoir is a large chalk field with well-preserved porosity of up to 50% in certain
234 parts of the field. The high porosity is due to the highly over-pressured reservoir units and, as
235 such, compaction provides the main drive mechanism for production. Compaction also plays
236 a critical role in field geomechanics: total subsidence currently exceeds 6 meters below the
237 central platforms. The Valhall hydro-mechanical model was developed and implemented to
238 predict future subsidence, assist drilling and optimize casing designs in the highly depleted
239 and compacted crest of Valhall field (see Table 1 for mechanical properties). Due to the
240 maturity of this field, the reservoir fluid-flow simulation models have been extensively history-
241 matched with production data and, three-dimensional full-field finite-element based
242 geomechanics model for overburden and reservoir has been history-matched with production
243 data (e.g., Kristiansen & Plischke, 2010). In this paper, the hydro-mechanical simulations for
244 Valhall involved coupling the ELFEN geomechanical simulator (Rockfield Software Ltd) with
245 the reservoir flow simulator VIP (Halliburton). The finite-element mesh was created using the
246 grid generator RMS/TEMPEST (Roxar Ltd) and consists of 30 layers created from the
247 geological model. The geomechanical mesh begins from the sea floor, but it includes the
248 water column loading. The ELFEN geomechanical simulation was performed using a
249 tetrahedral mesh of approximately 6 million finite elements and the VIP simulation was
250 performed using a finite-difference mesh of 0.5 million cells (see Figure 2). Since the ELFEN
251 and VIP mesh are different, parameters between meshes are transferred during the coupling

252 stage using a spatial mapping algorithm based on the least-squares method. The hydro-
253 mechanical model has been constrained by a range of field and surveillance data: GPS,
254 time-lapse seafloor bathymetry (Kristiansen & Plischke, 2010), radioactive markers in
255 reservoir and overburden, and time-lapse seismic.

256 [Figure 2 here]

257 The geomechanical model was initialized using in-situ geostatic stresses to establish the pre-
258 production status of the Valhall field. Specifically, the background geostatic stresses were
259 applied via a 1-D geostatic stress profile under the following conditions: (a) the vertical total
260 stresses are based on the gravitational forces and material bulk density, and are maintained
261 by the application of gravitational acceleration g ; (b) the pore pressure is assumed to be
262 hydrostatic with over-pressure if applicable (i.e. modeled according to measurements and
263 predictions of overpressure), and (c) horizontal effective stresses are assigned based on the
264 assigned k_0 ratios (ratio of vertical to lateral earth pressures) and the calculated vertical
265 effective stress or from initial fracture pressure measurements where available. The values of
266 $k_0=0.75$ and $k_0=0.5$ were used for the Tor and Hod reservoirs, respectively (Pattillo et al.,
267 1998; Kristiansen & Plischke, 2010). Following initialization, the hydro-mechanical response
268 due to production was simulated using a two-way coupling scheme, where the
269 geomechanical model used the pore pressure evolution calculated in the reservoir simulator
270 and the reservoir simulator used the updated pore volume change calculated in the
271 geomechanical simulator. For the over-, under- and side-burden, the pore pressure was kept
272 constant during the simulation in these cases.

273 [Table 1]

274 To map the hydro-mechanical results to seismic velocities, we used average microcrack
275 parameters inverted using chalk and shale core data (see Angus et al. 2009). The chalk data
276 used in Angus et al. (2009) is consistent with that present by Alam et al. (2012). For the
277 reservoir rocks, we used an initial crack density and initial aspect ratio of 0.25 and 0.0001,
278 respectively. For the non-reservoir rocks we used an initial crack density and initial aspect

279 ratio of 0.125 and 0.001. For this preliminary work, we did not have sufficient rock data to
280 justify using depth-dependent or anisotropic initial microcrack properties. However, even with
281 isotropic initial microcrack parameters, the rock physics model allows seismic anisotropy to
282 develop due to non-hydrostatic stress change (see Verdon et al. 2008). For the AVOA
283 predictions, we selected a sub-volume of the field (the south-east section of the crestal area),
284 where previously published 4D seismic anisotropy studies are available (e.g., Hall & Kendall
285 2003). Figure 3 shows the sub-volume with respect to finite-element model.

286 [Figure 3 here]

287 **4. Results**

288 The hydro-mechanical simulation is performed for both one-way and two-way coupling. In the
289 one-way coupling, pore pressures from the flow simulator are passed to the geomechanical
290 simulator and the reservoir flow simulator uses a table of pore volume multipliers. The table
291 is then used to update porosity within the flow simulation based on geomechanically
292 predicted pressure changes. In the two-way coupling, hydro-mechanical simulation is driven
293 by exchanging information between the reservoir flow simulator and the geomechanical
294 simulator: pore pressure and water saturation calculated in the reservoir simulator is passed
295 to the geomechanical simulator, the geomechanical simulator updates the pore volume and
296 passes this update back to the flow simulator. In both coupling cases, the hydro-mechanical
297 solution accounts to varying degrees of accuracy for the strain rate dependent reservoir
298 compaction during depletion, re-pressurization and water flooding. In this study, no effort was
299 made to history-match the two-way coupled model since this is a time consuming and more
300 challenging task than history-matching a one-way coupled model. However, time-lapse
301 seismic and microseismic data are another potential source of data that can be used to
302 improve geomechanical model calibration as well as improve two-way coupling by minimizing
303 misfit between prediction and observation.

304 **4.1 Subsidence**

305 [Figure 4 here]

306 Figure 4 compares the results of surface subsidence prediction using the one-way coupling
307 and the field measurement. The results show very good match with the observed data for the
308 evolution of vertical displacement predictions below the QP North and South platforms during
309 approximately 25 years production is shown.

310 **4.2 AVOA**

311 There have been several studies of azimuthal seismic anisotropy carried out for the Valhall
312 reservoir using the multicomponent ocean bottom seismic (OBS) array (Rosland et al. 1999,
313 Hall & Kendall 2003). The OBS array consisted of 4C cables with 600 m x 600 m cross-
314 spread, providing good azimuthal distribution. Olofsson et al. (2003) provided one of the
315 earliest seismic anisotropy studies, examining the crestal zone using P-to-S mode
316 conversions using data acquired in 1997-1998 with the 3D 4C OBS array. By performing
317 shear-wave splitting analysis of the mode conversions using a layer stripping method,
318 Olofsson et al. (2003) observed radial anisotropy in the near surface consistent with the
319 subsidence bowl as well as anisotropy patterns related to subsurface structure and fracture
320 systems. Using the same data, Hall & Kendall (2003) performed AVOA analysis on the
321 southeast section of the anticlinal structure and observed AVOA patterns consistent with
322 fracture distributions and faults within the reservoir. The length-scales of the fractures are
323 sub-seismic wavelengths (Hall & Kendall 2003), and so could be due to not only sub-seismic
324 scale fractures but also microcracks. However, recent analysis suggests that the AVOA
325 pattern is sensitive also to lithology and geometry, where some of the shear fractures act as
326 baffles to fluid-flow (Barkved 2012).

327 [Figure 5 here]

328 [Figure 6 here]

329 Figures 5-7 compare the predicted AVOA seismic response for a sub-volume of the field to
330 the previous published AVOA seismic results of Hall (2000). In Figure 5, the AVOA patterns
331 for the Base Miocene horizon show some consistency, with predominant anisotropy oriented

332 North-South. However, there is also significant anisotropy oriented East-West in the
333 observed data that is not predicted in the model. The results for the 2130ms horizon are
334 shown in Figure 6. The patterns also show some similarity, with predominant anisotropy
335 oriented approximately East-West. Both AVOA patterns show a wedge like pattern in the top-
336 left quadrant, whereas the circular pattern in the observed data at UTM Y 6.2353 and UTM X
337 5.258 appears further to the left in the model prediction. In Figure 7, the results for the Top
338 Chalk horizon are shown, where there is weaker similarity between the predicted and
339 observed AVOA response. There are weak circular patterns occurring within the right side of
340 the horizon. However, the orientation of dominant anisotropy shown in the polar plots are not
341 in agreement, with the observed data being oriented approximately East-West and the model
342 predictions oriented approximately North-South. It is encouraging that the initial model
343 predictions compare broadly with the seismic observations of anisotropy for these two
344 horizons considering that there was no calibration of the rock physics models to the Valhall
345 data and that we did not include sub-seismic fractures within the geomechanical model.

346 [Figure 7 here]

347 **4.3 Microseismicity**

348 We use the matrix failure approach of Angus et al. (2010) to predict microseismicity from the
349 hydro-mechanical simulation. A limit on the number of elements used in the finite-element
350 based geomechanical simulator means that the microseismic predictions are limited by the
351 continuum formulation (i.e., not localized). Although this approach cannot model the micro-
352 mechanical behaviour as can be done with discrete-element and particle-flow geomechanical
353 solutions, it does provide a first-order estimate of regions within the model that might
354 generate seismicity and potential the type of failure (tensile, shear or shear-enhanced
355 compaction). It is important to note that it is unlikely that tensile or shear-enhanced
356 compaction type events would be observable within reservoirs given the distance between
357 the event locations and the geophones, whereas shear-type events would be as they
358 generate much larger seismic energy. For realistic model geometries, proper geostatic

359 initialization and sufficiently accurate hydro-mechanical history matching using well data,
360 continuum based finite-element simulators should provide reasonable prediction of the stress
361 and strain evolution. As was seen in Figure 4, the accurate subsidence predictions suggest
362 that the evolution of strain within the model is not only globally reasonable but also locally on
363 the scale of the finite-element meshes. Since the Valhall model includes mechanical
364 anisotropy and subsurface structure, the microseismic predictions should represent plausible
365 first-order predictions of seismicity and their average mechanisms.

366 [Figure 8 here]

367 In Figure 8, the distribution of all shear-type microseismic events for the complete finite-
368 element mesh is shown (i.e., microseismic predictions are done for the whole hydro-
369 mechanical model and not limited to the seismic sub-volume). The lateral distribution of
370 events follows a north-west/south-east distribution consistent with the results of Zoback &
371 Zinke (2002) and follows the long-axis of the anticlinal reservoir structure. The shear-type
372 events are primarily localised between 2300 and 3000 m depth within the lower Balder
373 formation. Dyer et al (1999) examine microseismic data and observe depth distribution of
374 events between 2300 and 2400 m, which is consistent with our predictions for the sub-
375 volume that they examine.

376 [Figure 9 here]

377 In Figure 9, the predicted moment tensor mechanisms are plotted using the geometrical
378 representation of Tape & Tape (2012). The predicted shear-type solutions fall within
379 plausible mechanisms, with many events being predominantly double-couple failure as well
380 as both positive and negative linear vector dipole failure indicative of volumetric components.
381 The predicted double-couple mechanisms are predominantly normal fault type, which is
382 consistent with the composite double-couple solution of Zoback & Zinke (2002).

383 **Conclusions**

384 The integrated geomechanical, fluid-flow and seismic modelling workflow has shown promise
385 in predicting several manifestations of geomechanical deformation. The results of the surface
386 subsidence predictions compare very well with field observations. Using a non-linear rock
387 physics model calibrated with core data, the predicted AVOA response closely resembles
388 that measured from field seismic data. This result is very encouraging given that there was
389 no further calibration of the rock physics model to Valhall specific core data or the Valhall
390 hydro-mechanical simulation. The spatial pattern of modelled microseismicity is consistent
391 with previously published microseismic analyses and the modelled failure mechanisms are
392 consistent with typical reservoir induced seismicity (e.g., predominantly double couple failure
393 with variable volumetric component). The results of this study suggest that seismic data can
394 be used to improve hydro-mechanical model calibration, which can be significant since
395 seismic data provide greater control over a much larger volume of the hydro-mechanical
396 model. Furthermore, integrated seismic and hydro-mechanical model can improve the non-
397 uniqueness of time-lapse seismic interpretation, for instance leading to identification of
398 reservoir volumes for infill drilling and also predicting stress changes for optimising hydraulic
399 fracturing. The next steps involve using seismic data to calibrate hydro-mechanical models,
400 such as uncertainty in rock physics models (e.g., intrinsic anisotropy, static-to-dynamic
401 elastic conversion, calibration of input model parameters and in-situ stress sensitivity). As
402 well, temporal variations in shear-wave anisotropy (Teanby et al. 2004) and multiplet
403 behaviour of fault failure (de Meersman et al. 2009) from microseismic data could be used to
404 further constrain the hydro-mechanical models.

405 **Acknowledgements**

406 The authors would like to thank the sponsors of the ITF joint-industry projects IPEGG (BG,
407 BP, ENI and Statoil) and GESER (Shell, ConocoPhillips, Chevron and DECC). We thank
408 Rockfield Software for access to the geomechanical simulator ELFEN, and Roxar for access
409 to the geological model builder RMS (TEMPEST), and Halliburton for access to VIP. The

410 Valhall license (BP Norge AS and Hess Norge AS) is thanked for permission to publish this
411 research.

412 References

- 413 Alassi, H., R. Holt and M. Landro (2010) Relating 4D seismics to reservoir geomechanical changes
414 using a discrete element approach, *Geophysical Prospecting*, **58**, 657-668.
- 415 Alam, M.M., I.L. Fabricius and H.F. Christensen (2012) Static and dynamic effective stress coefficient
416 of chalk, *Geophysics*, **77**(2), L1-L11.
- 417 Angus, D.A., Q.J. Fisher and J.P. Verdon (2012) Exploring trends in microcrack properties of
418 sedimentary rocks: An audit of dry and water saturated sandstone core velocity-stress
419 measurements, *International Journal of Geosciences*, **3**, 822-833.
- 420 Angus, D.A., J-M. Kendall, Q.J. Fisher, J.M. Segura, S. Skachkov, A.J.L. Crook and M. Dutko (2010)
421 Modelling microseismicity of a producing reservoir from coupled fluid-flow and geomechanical
422 simulation, *Geophysical Prospecting*, **58**(5), 901-914.
- 423 Angus, D.A. and C.J. Thomson (2012) Modelling converted seismic waveforms in isotropic and
424 anisotropic 1-D gradients: discontinuous versus continuous gradient representations, *Studia*
425 *Geophysica et Geodaetica*, **56**, 383-409.
- 426 Angus, D.A., J.P. Verdon, Q.J. Fisher and J-M. Kendall (2009) Exploring trends in microcrack
427 properties of sedimentary rocks: An audit of dry-core velocity-stress measurements, *Geophysics*, **74**,
428 E193-E203.
- 429 Angus, D.A., J.P. Verdon, Q.J. Fisher, J-M. Kendall, J.M. Segura, T.G. Kristiansen, A.J.L. Crook, S.
430 Skachkov, J. Yu and M. Dutko (2011) Integrated fluid-flow, geomechanical and seismic modelling for
431 reservoir characterization, *Recorder*, Canadian Society of Exploration Geophysicists, **36**(4), 18-27.
- 432 Aziz, K and A. Settari (1979) *Petroleum reservoir simulation*, Applied Science Publishers Ltd., London.
- 433 Barkved, O., Heavy, P., Kjeldstadli, R., Kleppan, T., and Kristiansen, T.G. [2003] Valhall Field – Still
434 on Plateau after 20 Years of Production, SPE 83957.
- 435 Barkved, O.I. and Kristiansen, T. [2005] Seismic time-lapse effects and stress changes: Examples
436 from a compacting reservoir. *The Leading Edge*, December, 1244-1248.
- 437 Barkved, O.I. (2012) *Seismic surveillance for reservoir delivery: From a practitioner's point of view*,
438 Volume 6 of Education tour series, European Association of Geoscientists and Engineers.
- 439 Brown, R.J.S. and J. Korringa (1975) On the dependence of the elastic properties of a porous rock on
440 the compressibility of the pore fluid, *Geophysics*, **40**, 608-616.
- 441 Calvert, R. (2005) Insights and methods for 4D reservoir monitoring and characterization,
442 Distinguished Instructor Series No.8, EAGE.
- 443 Chapman, M. (2003) Frequency-dependent anisotropy due to meso-scale fractures in the presence of
444 equant porosity, *Geophysical Prospecting*, **51**, 369-379.
- 445 Crook, A.J.L., J.-G. Yu and S.M. Willson (2002) Development of an orthotropic 3D elasticplastic
446 material model for shale, *Society of Petroleum Engineers*, 78238.
- 447 Crook, A.J.L., S. M. Willson, J-G. Yu and D.R.J. Owen (2006) Predictive modelling of structure
448 evolution in sandbox experiments, *Journal of Structural Geology*, **28**, 729-744.
- 449 Crook, A.J.L., Yu, J.G., Flatebø, R.E. and Kristiansen, T.G. 2008, Computational modelling of the rate
450 dependent deformation and liquefaction of chalk, ARMA 08-176, the 42nd US Rock Mechanics
451 Symposium and 2nd U.S.-Canada Rock Mechanics Symposium, held in San Francisco, June 29-
452 July 2, 2008.
- 453 Dean, R.H., X. Gai, C.M. Stone and S.E. Minkoff (2003) A comparison of techniques for coupling
454 porous flow and geomechanics, *Society of Petroleum Engineers*, 79709.
- 455 De Meersman, K., J-M. Kendall and M. Van Der Baan (2009) The 1998 Valhall microseismicity: An
456 integrated study of relocated sources, seismic multiplets and S-wave splitting,
457 *Geophysics*, **74**(5), 183 – 195.
- 458 Dewhurst, D.N. and A.F. Siggins (2006) Impact of fabric, microcracks and stress field on shale
459 anisotropy, *Geophysical Journal International*, **165**, 135-148.
- 460 Dyer, B.C., R.H. Jones, J.F. Cowles, O. Barkved and P.G. Folstad (1999) Microseismic survey of a
461 North Sea reservoir, *World Oil*, **220**, 74–78.
- 462 Ferronato, M., Castelletto, N., Gambolati, G., Janna, C. and Teatini, P. (2013) II cycle compressibility
463 from satellite measurements, *Geotechnique*, **63**(6), 479-486.
- 464 Fjær, E. and Kristiansen, T.G., 2009, An Integrated Geomechanics, Rock Physics and Seismic Model,
465 71st EAGE Conference & Exhibition — Amsterdam, The Netherlands, 8 - 11 June 2009.

466 Fuck, R.F., and I. Tsvankin (2009) Analysis of the symmetry of a stressed medium using nonlinear
467 elasticity, *Geophysics*, **74**(5), WB79-WB87.

468 Fuck, R.F., Tsvankin, I. and Bakulin, A. (2011) Influence of background heterogeneity on travelttime
469 shifts for compacting reservoirs, *Geophysical Prospecting*, **59**, 78–89.

470 Geertsma, J. (1973) Land subsidence above compacting oil and gas reservoirs, *Journal of Petroleum*
471 *Geology*, **25**(6), 734-744.

472 Gutierrez, M.R. and W. Lewis (1998) The role of geomechanics in reservoir simulation, *Proceedings of*
473 *Euro '98*, **2**, 439-448.

474 Hall, S.A. (2000) Rock Fracture Characterisation and Seismic Anisotropy: Application to ocean bottom
475 seismic data, PhD thesis, University of Leeds, Leeds, UK.

476 Hall, S.A. and J-M. Kendall (2000) Constraining the interpretation of AVOA for fracture
477 characterisation, *Proceedings of the Ninth International Workshop on Seismic Anisotropy:*
478 *Anisotropy 2000: Fractures, Converted Waves and Case Studies*, Society of Exploration
479 Geophysicists, 107–144.

480 Hall, S.A. and J-M. Kendall (2003) Fracture characterization at Valhall: Application of P-wave
481 amplitude variation with offset and azimuth (AVOA) analysis to a 3D ocean-bottom data set,
482 *Geophysics*, **68**(4), 1150-1160.

483 Hall, S.A., J-M. Kendall, J. Maddock and Q.J. Fisher (2008) Crack density tensor inversion for analysis
484 of changes in rock frame architecture, *Geophysical Journal International*, **173**, 577-592.

485 Hatchell, P.J. and S. Bourne (2005) Rocks under strain: Strain-induced time-lapse time shifts are
486 observed for depleting reservoirs, *The Leading Edge*, **24**, 1222-1225.

487 He, Y., Angus, D.A., Clark, R.A. & Hildyard, M.W. (2015) Analysis of time-lapse travel-time and
488 amplitude changes to assess reservoir compartmentalisation, *Geophysical Prospecting*.

489 Helbig, K. and P.N.J. Rasolofosaon (2000) A theoretical paradigm for describing hysteresis and
490 nonlinear elasticity in arbitrary anisotropic rocks, *Proceedings of the Ninth International Workshop on*
491 *Seismic Anisotropy: Anisotropy 2000: Fractures, Converted Waves and Case Studies*, Society of
492 Exploration Geophysicists.

493 Herwanger, J.V. and S.A. Horne (2005) Predicting time-lapse stress effects in seismic data, *The*
494 *Leading Edge*, **24**, 1234-1242.

495 Herwanger, J.V. and S.A. Horne (2009) Linking reservoir geomechanics and time-lapse seismics:
496 Predicting anisotropic velocity changes and seismic attributes, *Geophysics*, **74**(4), W13-W33.

497 Herwanger, J.V., C.R. Schitt, R. Frederiksen, F. If, O.V. Vejlbk, R. Wold, H.J. Hansen, E. Palmer and
498 N. Koutsabeloulis (2010) Applying time-lapse seismic to reservoir management and field
499 development planning at South Arne, Danish North Sea, in Vining, B.A. and S.C. Pickering (eds)
500 *Petroleum Geology: From Mature Basins to New Frontiers*, *Proceedings of the 7th Petroleum*
501 *Geology Conference*.

502 Hillis, R.R. (2001) Coupled changed in pore pressures and stress in oil fields and sedimentary basins,
503 *Petroleum Geoscience*, **7**(4), 419-425.

504 Hueckel, T., Cassiani, G., Tao, F., Pellegrino, A. and Fioravante, V. (2001) Effect of aging on
505 compressibility of gas/oil bearing sediments and their subsidence, *ASCE Journal of Geotechnical*
506 *and Geoenvironmental Engineering*, **127**(11), 926-938.

507 Jenner, E. (2002) Azimuthal AVO: Methodology and data examples, *The Leading Edge*, **21**, 782-786.

508 Johnson, D.H. (2013) Practical applications of time-lapse seismic data, *Distinguished Instructor*
509 *Series*, No. 16, EAGE.

510 Johnson, P.A. and P.N.J. Rasolofosaon (1996) Manifestation of nonlinear elasticity in rock: Convincing
511 evidence over large frequency and strain intervals from laboratory studies, *Nonlinear Processes in*
512 *Geophysics*, **3**, 77-88.

513 Kendall, J-M., Q.J. Fisher, S. Covey-Crump, J. Maddock, A. Carter, S.A. Hall, J. Wookey, S.L.A.
514 Valcke, M. Casey, G. Lloyd and W. Ben Ismail (2007) Seismic anisotropy as an indicator of reservoir
515 quality in siliciclastic rocks, in *Structurally Complex Reservoirs (Special Publication 292)*, eds. Jolley,
516 S.J., D. Barr, J.J. Walsh and R. Knipe. Geological Society, 123-136.

517 Kristiansen, T.G. and B. Plischke (2010) History matched full field geomechanics model of the Valhall
518 Field including water weakening and re-pressurisation, *SPE*, 131505.

519 Kristiansen, T.G., Barkved, O.I., Buer, K. and Bakke, R. [2005] Production Induced Deformations
520 Outside the Reservoir and Their Impact on 4D Seismic. *International Petroleum Technology*
521 *Conference*, Doha, Qatar, 21–23 November, paper IPTC 10818.

522 Kristiansen, T.G. and Flatebø, R.E. [2009] 60 Days Ahead of Schedule -Reducing Drilling Risk at
523 Valhall Using Computational Geomechanics. *SPE/IADC Drilling Conference and Exhibition*,
524 Amsterdam, The Netherlands, 17–19 March, paper SPE/IADC 119509.

525 Minkoff, S.E., C.M. Stone, S. Bryant, M. Peszynska and M.F. Wheeler (2003) Coupled fluid flow and
526 geomechanical deformation modeling, *Journal of Petroleum Science and Engineering*, **38**, 37-56.
527 Minkoff, S.E., C.M. Stone, S. Bryant and M. Peszynska (2004) Coupled geomechanics and flow
528 simulation for time-lapse seismic modeling, *Geophysics*, **69**(1), 200-211.
529 Nur, A. and G. Simmons (1969) Stress-induced velocity anisotropy in rock: An experimental study,
530 *Journal of Geophysical Research*, **74**, 6667-6674.
531 Olden, P., P. Corbett, R. Westerman, J. Somerville, N. Koutsabeloulis and B. Smart (2001) Modelling
532 combined fluid and stress change effects in the seismic response of a producing hydrocarbon
533 reservoir, *The Leading Edge*, **20**, 1154-1163.
534 Olofsson, B., T. Probert, J.H. Kommedal, and O.I. Barkved (2003) Azimuthal anisotropy from the
535 Valhall 4C 3D survey, *The Leading Edge*, **22**, 1228-1235.
536 Pattillo, P.D, Kristiansen, T.G., Sund, G.V., and Kjeldstadli, R.M. (1998) Reservoir Compaction and
537 Seafloor Subsidence at Valhall, *Proc. Eurock '98*, Trondheim, Norway, SPE/ISRM 47274.
538 Prioul, R., A. Bakulin and V. Bakulin (2004) Nonlinear rock physics model for estimation of 3D
539 subsurface stress in anisotropic formations: Theory and laboratory verification, *Geophysics*, **69**, 415-
540 425.
541 Rosland, B., E.L. Tree and P. Kristiansen (1999) Acquisition of 3D/4C OBS data at Valhall, 61st Annual
542 Meeting EAGE, Expanded Abstract, E050.
543 Ruger, A. (1998) Variation of P-wave reflectivity with offset and azimuth in anisotropic media,
544 *Geophysics*, **63**, 935-947.
545 Rutqvist, J. (1995) Determination of hydraulic normal stiffness of fractures in hard rock from hydraulic
546 well testing, *International Journal of Rock Mechanics, Mining Science & Geomechanics*, **32**: 513-
547 523.
548 Rutqvist, J., Y-S. Wu, C.F. Tsang and G. Bodvarsson (2002) A modeling approach for analysis of
549 coupled multiphase fluid flow heat transfer, and deformation in fractured porous rock, *International*
550 *Journal of Rock Mechanics & Mining Sciences*, **39**, 429-442.
551 Sayers, C.M. (2007) Asymmetry in the time-lapse seismic response to injection and depletion,
552 *Geophysical Prospecting*, **55**(5), 699-705.
553 Sayers, C. and Kachanov, M. (1995) Microcrack-induced elastic wave anisotropy of brittle rocks,
554 *Journal of Geophysical Research*, **100**(B3), 4149-4156.
555 Schoenball, M., T.M. Muller, B.I.R. Muller and O. Heidbach (2010) Fluid-induced microseismicity in
556 pre-stressed rock masses, *Geophysical Journal International*, **180**, 813-819.
557 Schoenberg, M. and Sayers, C. (1995) Seismic anisotropy of fractured rock, *Geophysics*, **60**(1), 204-
558 211.
559 Schubnel, A. and Gueguen, Y. (2003) Dispersion and anisotropy of elastic waves in cracked rocks,
560 *Journal of Geophysical Research*, **108**(B2), p. 15.
561 Segall, P. (1989) Earthquakes triggered by fluid extraction, *Geology*, **17**, 942-946.
562 Segura, J.M., Q.J. Fisher, A.J.L. Crook, M. Dutko, J. Yu, S. Skachkov, D.A. Angus, J.P. Verdon and J-
563 M. Kendall (2011) Reservoir stress path characterization and its implications for fluid-flow production
564 simulation, *Petroleum Geoscience*, **17**, 335-344.
565 Tape, W. and C. Tape (2012) A geometric setting for moment tensors, *Geophysical Journal*
566 *International*, **190**(1), 476-498.
567 Teanby, N., M. Van der Baan and J-M. Kendall (2004) Automation of Shear-Wave Splitting
568 Measurements using Cluster Analysis, *Bulletin of the Seismological Society of America*, **94**(2), 453-
569 463.
570 Tod, S. (2002) The effects of stress and fluid pressure on the anisotropy of interconnected cracks,
571 *Geophysical Journal International*, **149**(1), 149-156.
572 Trudeng, T., X. Garcia-Teijeiro, A. Rodrigues-Herrera and J. Khazanehdari (2014) Using stochastic
573 seismic inversion as input for 3D geomechanical models, *International Petroleum Technology*
574 *Conference*, 17547.
575 Valcke, S., M. Casey, G. Lloyd, J-M. Kendall and Q.J. Fisher (2005) Seismic anisotropy in
576 sedimentary rocks, *Geophysical Journal International*, **166**, 652-666.
577 Verdon, J.P., D.A. Angus, J-M. Kendall and S.A. Hall (2008) The effects of microstructure and
578 nonlinear stress on anisotropic seismic velocities, *Geophysics*, **73**(4), D41-D51.
579 Verdon, JP, J-M. Kendall, D.J. White and D.A. Angus (2011) Linking microseismic event observations
580 with geomechanical models to minimise the risks of storing CO₂ in geological formations, *Earth and*
581 *Planetary Science Letters*, **305**, 143-152.
582 Zoback, M.D. and J.C. Zinke (2002) Production-induced normal faulting in the Valhall and Ekofisk oil
583 fields, *Pure and Applied Geophysics*, **159**, 403-420.
584

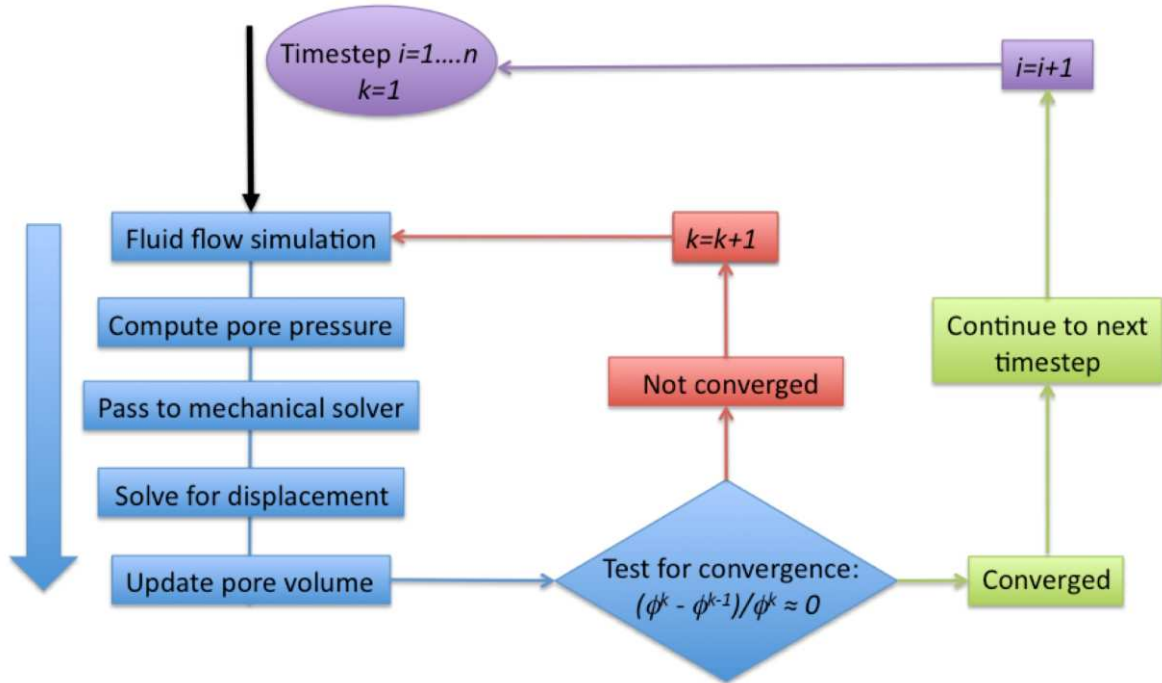
586 **Tables:**

Layer		E _x :E _y		E _z	ν _{xy}		ν _{xz} :ν _{yz}		G _{xy}	G _{xz} :G _{yz}		ε _i	a ₀	
		E ₁	E ₂		ν ₁	ν ₂	G ₁	G ₂				(x10 ⁴)		
Overburden	1	T200		240	150	0.25	0.15	96	55					
	2	T180		300	180	0.25	0.15	120	66					
	3	Intra mid Miocene		400	240	0.25	0.15	160	88	0.250		1		
	4	T110		500	300	0.25	0.15	200	110	0.245		1		
	5	Intra late Oligocene		650	390	0.25	0.15	260	130	0.240		1		
	6	Intra late Eocene		700	420	0.25	0.15	280	154	0.238		1		
	7	Early Eocene		750	450	0.25	0.15	300	165	0.238		1		
	8	-		=	=	=	=	=	=	=	=	=	=	
	9	Balder		2000	600	0.25	0.10	800	200	0.197		1		
	10	Sele		1100	900	0.30	0.20	423	360	0.227		1		
	11	Lista		1200	1000	0.30	0.20	461	360	0.224		1		
Reservoir & Side-burden	12 to 19	Tor		E=1000φ ^{-1.1}		0.175		X		0.230		10		
	20 to 24	Hod												
Under-burden	26 to 27	Chalk		7000		0.170		X		0.033		1		
	28 to 29	Shale		7000	4000	0.20	0.10	2917	1500	0.033		1		
	30	Shale		8000	6000	0.20	0.10	3333	2500	0.033		1		
Faults	31 to 60	Reservoir		E=900φ ^{-1.1}		0.25		X		0.230		1		
	61 to 90	Overburden		300		0.30		x		0.005		1		

587 **Table 1** Mechanical properties for the 30-layer Valhall model, where E is Young's modulus, ν is
588 Poisson's ratio, G is shear modulus, and φ is porosity [properties of the overburden and reservoir
589 were published in Kristiansen & Plischke (2010) and based on the work of Wittke (1990)]. Orthotropic
590 anisotropy (or vertical transverse isotropy) is incorporated, where the Cartesian coordinates are
591 defined with z being depth and x,y being lateral coordinates. The overburden (layers 1-11) is modelled
592 as an orthotropic linear elastic material. The reservoir sections (layers 12-24) are modelled as an
593 isotropic poro-elasto-plastic material. The upper section of the under-burden (layers 26 and 27) is
594 modelled using a linear elastic material behaviour, whereas the lower section (layers 28-30) is
595 modelled using an orthotropic linear elastic material behaviour.

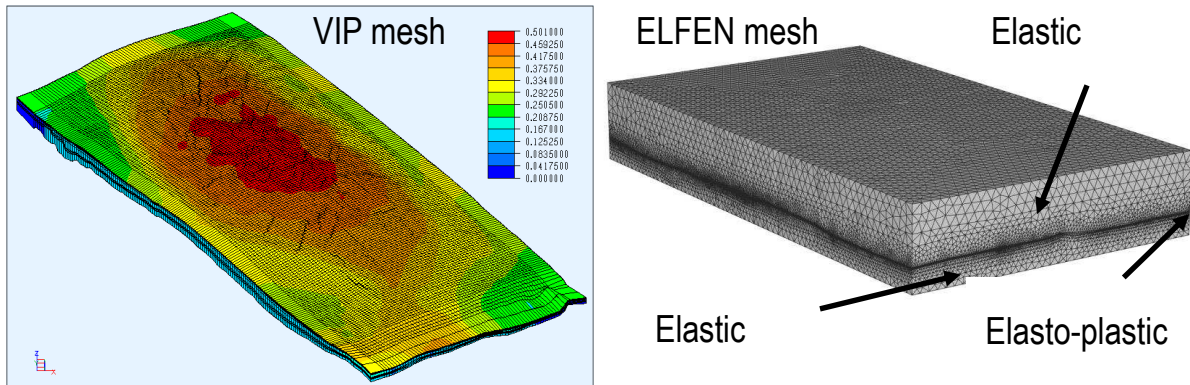
596

597 **Figures:**
598



599 **Figure 1** Diagram showing the iterative coupling between the fluid flow and geomechanical simulators.
600 At each time step the flow simulator computes the pore pressure and fluid properties, which are
601 subsequently passed to the geomechanical simulator to compute deformation. The geomechanical
602 simulator computes changes in porosity, which is returned to the flow simulator to recompute pore
603 pressures using the updated pore volumes. This iterative process, passing pore pressures and pore
604 volumes between the mechanical and flow simulators, is iterated until a stable value for porosity (and
605 a corresponding value for pore pressure) is reached, at which point the simulation moves to the
606 subsequent time-step.
607
608

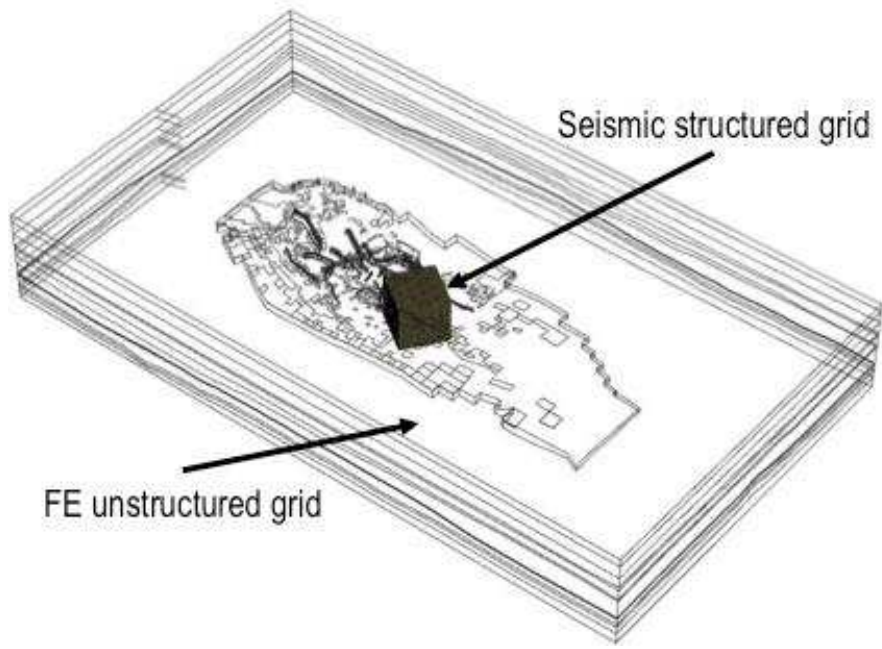
609



610

611 **Figure 2** Left: VIP reservoir flow model defined by finite-difference mesh consisting of 0.5 million cells,
612 having dimensions 19 km x 8 km laterally and 600 m in thickness. The colour contours represent
613 reservoir porosity, ranging from 0.0 (blue) to 0.5 (red). Right: ELFEN geomechanical model for Valhall
614 consisting of 6 million tetrahedral finite-elements, having lateral extent of 16 km x 28 km and depth
615 extent of 4.2 km. The reservoir is located at 2500 m depth (as shown by the dense layer of finite-
616 elements).

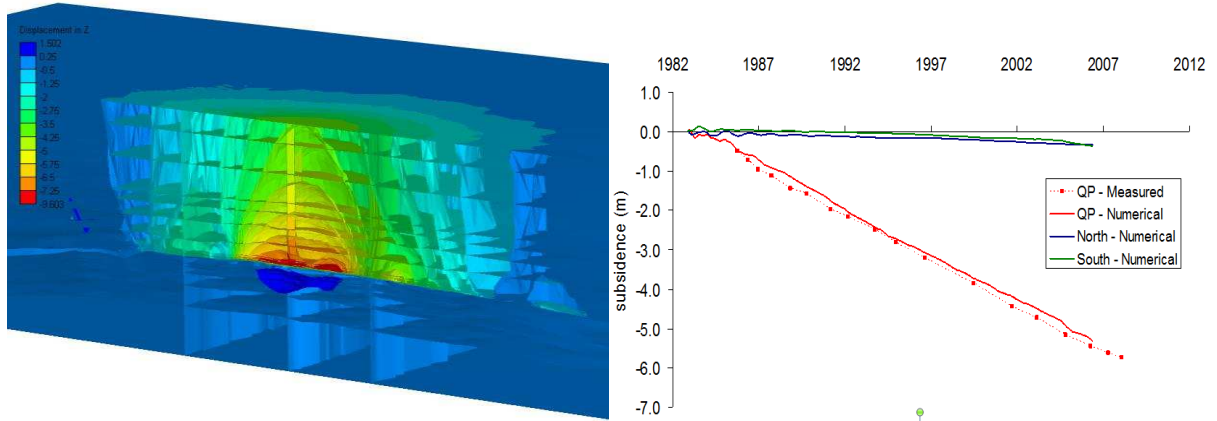
617



618
619 **Figure 3** Location of the seismic grid sub-volume within the finite-element geomechanical mesh. The
620 seismic grid has dimensions 2 km x 2 km laterally and 3.5 km in depth. The discrete grid consists of
621 50 x 50 lateral cells (lateral grid increment of 40 m) and 150 cells vertically (depth increment of 20 m).

622

623



624

625

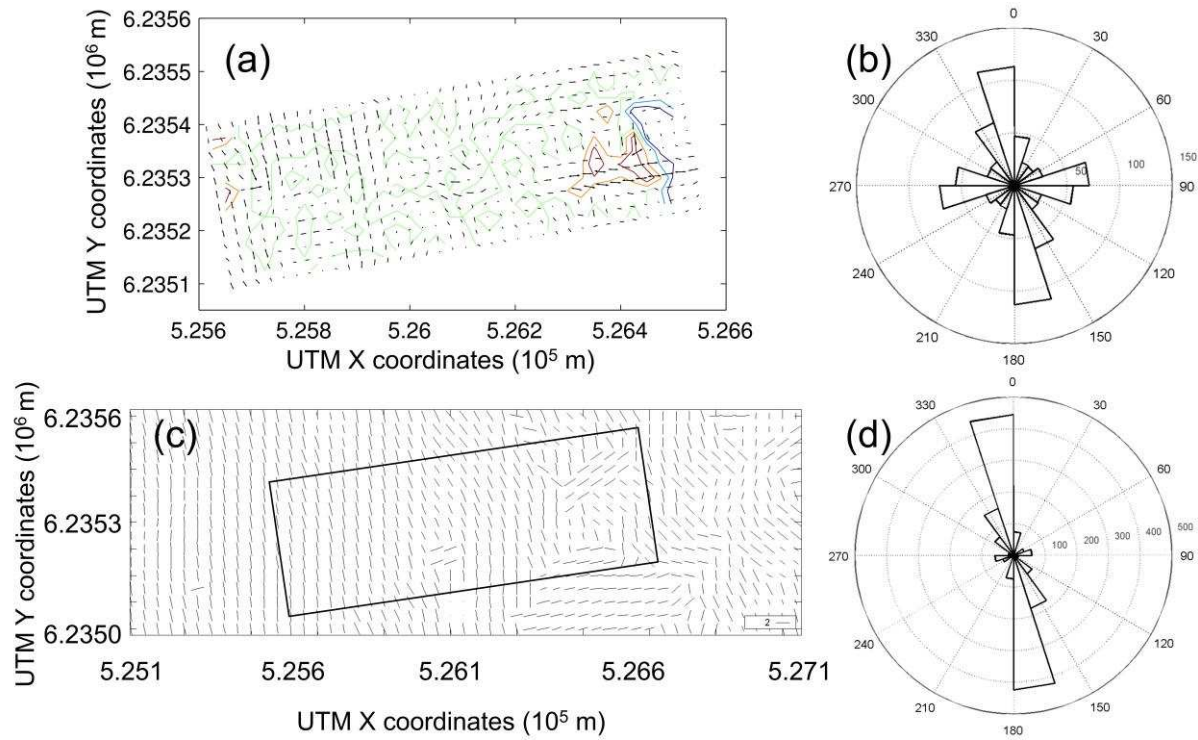
626

627

628

629

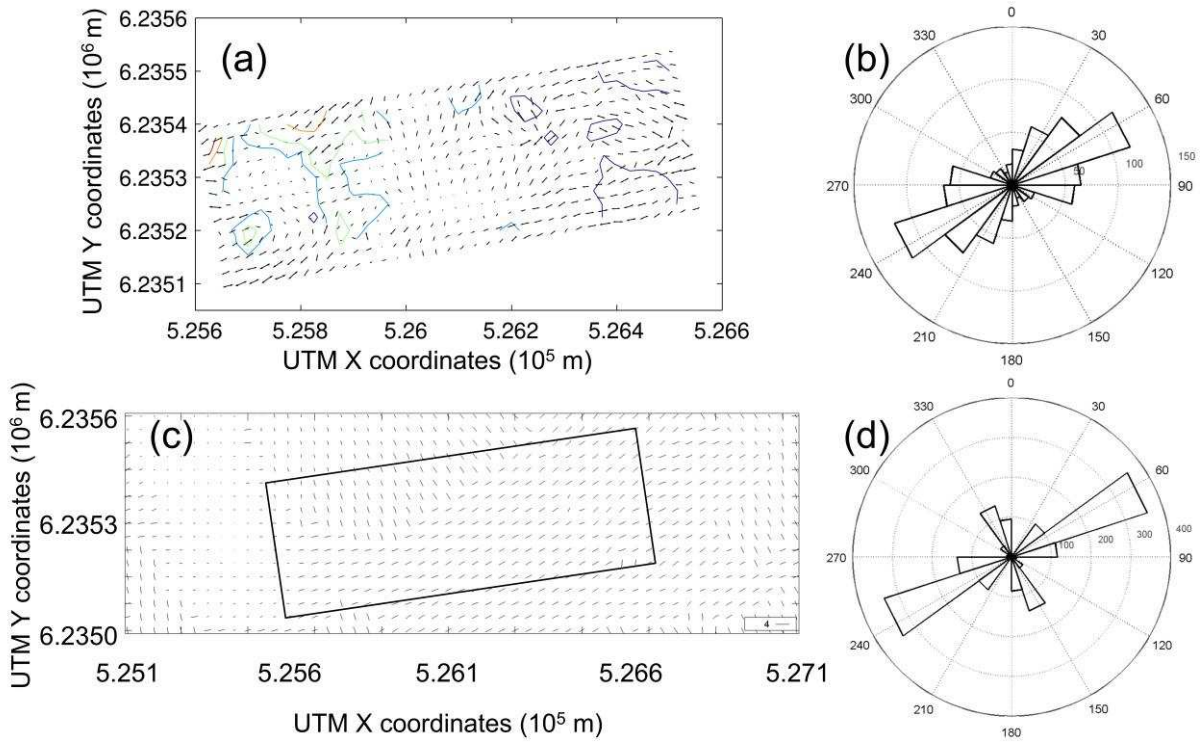
Figure 4 Left: Vertical section through the Valhall model showing the predicted vertical displacement isosurfaces, ranging from +1.5 (blue) to -9.0 (red). Right: Evolution of vertical displacement predictions of the sea floor surface below the QP platforms. GPS subsidence measurements are only available for the QP platform and not the North and South flank platforms.



630
 631
 632
 633
 634
 635
 636

Figure 5 Comparison of the observed (Hall 2000) and predicted AVOA response at Valhall for the Base Miocene horizon: (a) observed AVOA pattern, (b) polar area diagram showing the dominant orientation of the AVOA anisotropy for the observed data, (c) predicted AVOA pattern (note the area within rectangle approximately corresponds to the observed data), and (d) polar area diagram showing the dominant orientation of the AVOA anisotropy for the predicted data.

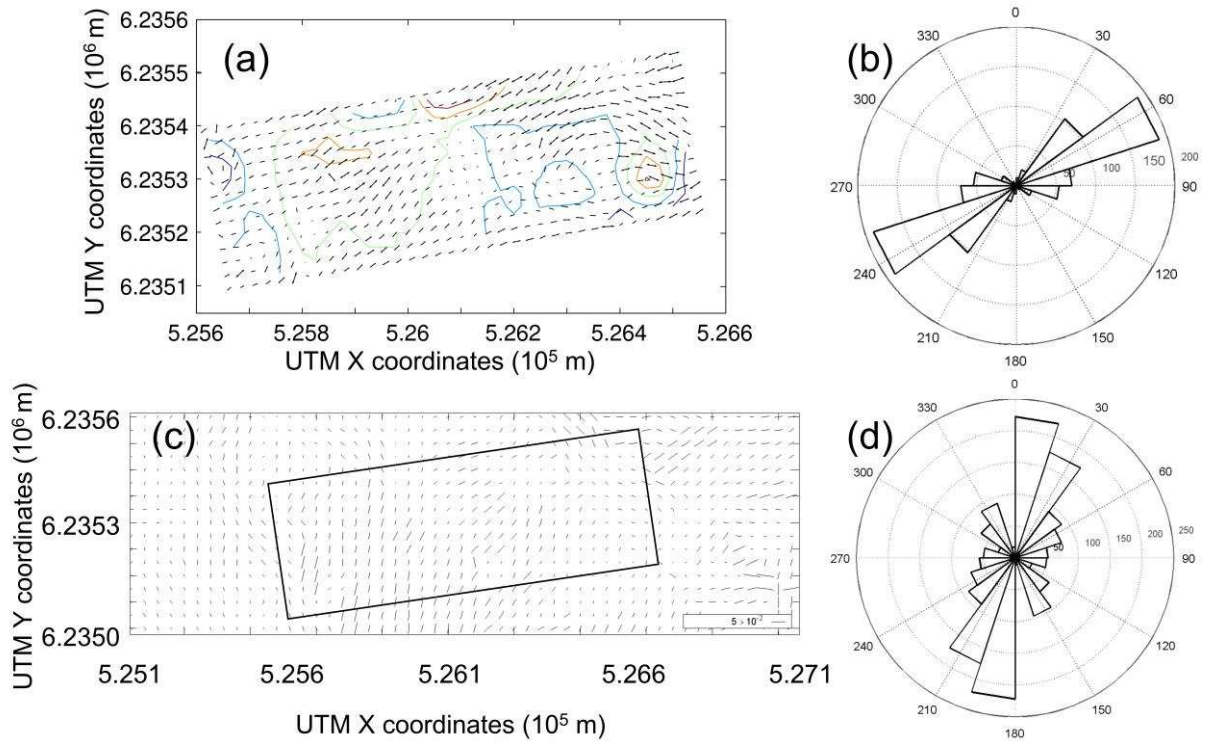
637



638
639
640
641

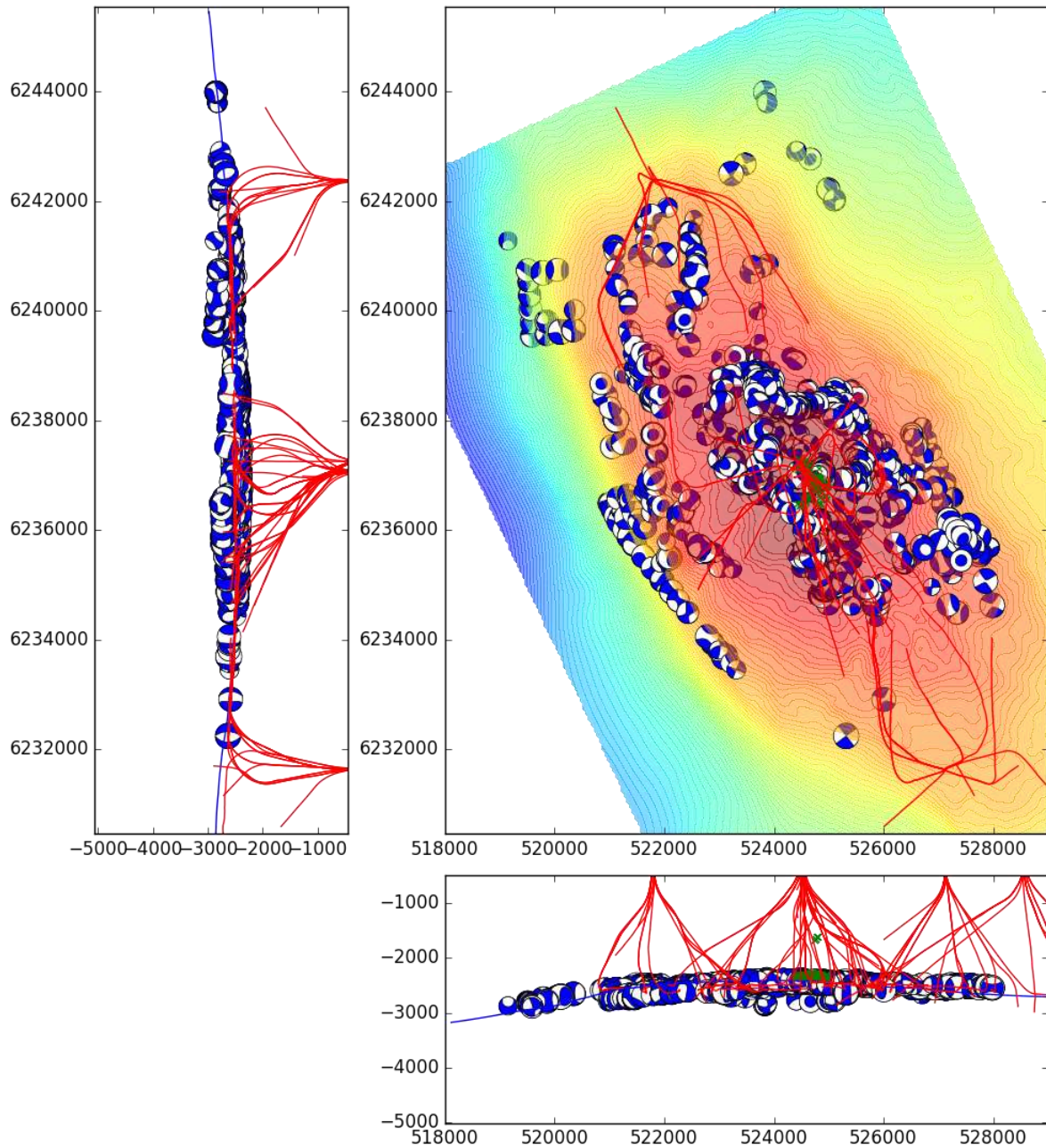
Figure 6 Comparison of the observed (Hall 2000) and predicted AVOA response at Valhall for the 2130ms horizon (see Figure 5 for details).

642



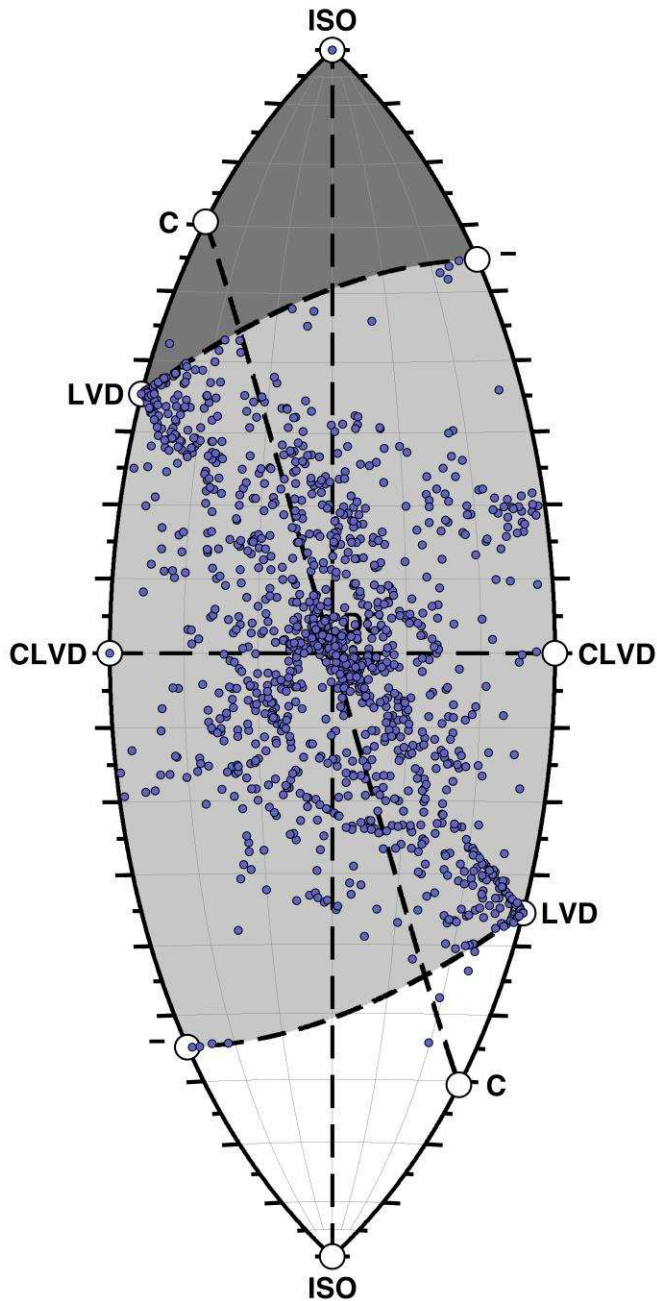
643
644
645
646
647

Figure 7 Comparison of the observed (Hall 2000) and predicted AVOA response at Valhall for the Top Chalk horizon (see Figure 5 for details). Although the azimuthal pattern of anisotropy is a poor fit, the relative magnitude of anisotropy is more consistent.



649
 650
 651
 652
 653
 654
 655
 656
 657

Figure 8 Predicted shear-type microseismic events (focal solutions are plotted using Harvard CMT with zero trace) for the 25 years of production. The size of the focal sphere indicates the relative magnitude of the predicted event [see Angus et al. (2010) for details of how the mechanisms and magnitudes are calculated]. The top of the reservoir is shown by the blue surface (in the vertical sections) and as a contour (in map view) with red depicting the anticline structure. The green symbols are the location of the observed microseismic events (Zoback & Zinke, 2002) and the red lines represents the location of the wellbore trajectories.

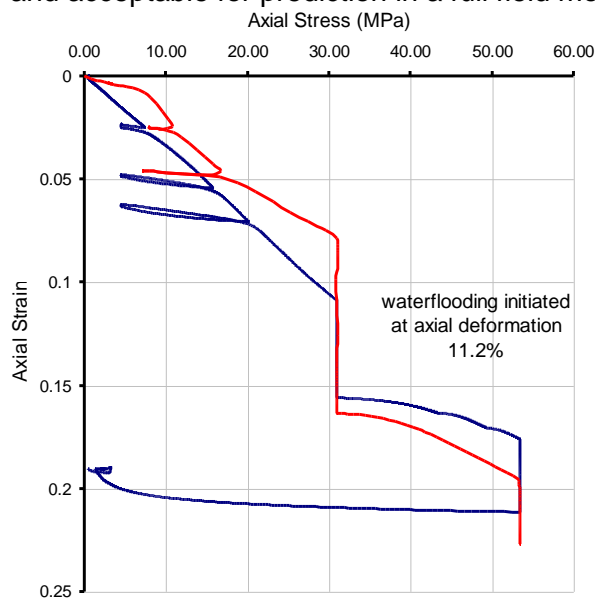


658
 659 **Figure 9** Predicted shear-type mechanism of the moment tensor solutions are plotted and are
 660 consistent with other observed reservoir microseismic mechanisms (Tape & Tape, 2012). In this
 661 figure, ISO represents explosive (top dark grey shaded region) and implosive (bottom white shaded
 662 region) failure, LVD represents linear vector dipole failure, CLVD represents compensated linear
 663 vector dipole failure, and C represents crack (tensile crack) failure. Double-couple shear failure is
 664 located in the center of the figure at the intersection of the horizontal line joining the CLVD
 665 mechanisms and the vertical line joining the ISO mechanisms. All the shear-type events fall within the
 666 region of expected shear type failure (light grey shaded region).
 667

668 Appendix A: Constitutive and rock physics models

669 A1: Constitutive model

670
671 We have adapted the existing ELFEN Soft Rock 3 constitutive (SR3) model (Crook et al.
672 2002; 2006) to predict liquefaction of chalk (Crook et al. 2008). The SR3 model is a Cam-
673 Clay type of model, which is strain rate dependent and so it takes into account time
674 dependent deformations, or creep. An additional feature within the SR3 model was
675 developed for Valhall allowing for water weakening within the Chalk. This feature was
676 developed in a way so that the yield surface properties are dependent on the change in
677 water saturation compared to a reference state. Figure A1 show examples of data from
678 laboratory water-flood experiments on Valhall chalk as well as the prediction of the water
679 weakening response based on the model developed in ELFEN. The results are very good
680 and acceptable for prediction in a full field model.



681
682 **Figure A1** Comparison of laboratory tests showing loading/unloading cycles and water weakening of
683 Valhall chalk and numerical modeling based on the extended SR3 model in ELFEN. The blue line is
684 the experimental data and the red line is the modelled data.

685 The Young's modulus has the following dependency

$$686 E = 46e^{-8.25\phi_{NI}},$$

687 where ϕ_{NI} represents the initial porosity and is in units of GPa. This dependency describes
688 the deformation of the rock mass and reflects the influence of fractures, local porosity
689 variation and heterogeneity, and as such is smaller than moduli measured from intact core
690 samples. More detail on the material properties is provided in Kristiansen & Plischke (2010).

691 692 A2: Rock physics model

693
694 To enable forward modelling of time-lapse seismic effects related to perturbations in
695 stresses, Verdon et al. (2008) extended the analytic effective medium formulation of Tod
696 (2002) to predict ultrasonic anisotropic and stress-dependent velocities. Specifically, the
697 analytic microcrack model introduces initial microcrack aspect ratio and number crack
698 density to predict stress dependence and crack-induced elastic anisotropy. The number
699 crack density is written

$$700
701 \epsilon_i(\sigma_{ii}^e) = \epsilon_i^0 e^{-c_r \sigma_{ii}^e},$$

702
703 where
704

$$705 \quad c_r = \frac{1}{\pi \mu_i a_i^o} \left(\frac{\lambda_i + 2\mu_i}{\lambda_i + \mu_i} \right)$$

706
707 ϵ_i^o and a_i^o are the effective initial number crack density and effective initial aspect ratio, λ_i
708 and μ_i are the Lamé constants, and σ_{ii}^e is the principal effective stress in the i -th direction.
709 The second-rank microcrack density term is

$$710 \quad a_{ii} = \frac{\epsilon_i}{h_i},$$

711
712 where
713
714

$$715 \quad h_i = \frac{3E_i^o}{32} \left(\frac{2 - \nu_i^o}{1 - (\nu_i^o)^2} \right)$$

716
717 is a normalization factor (Schubnel and Gueguen, 2003), and E_i^o and ν_i^o are the anisotropic
718 intact rock Young' modulus and Poisson ratio. This derivation yields an expression for the
719 effective elasticity that can model stress-induced elastic anisotropy due to deviatoric stress
720 fields. The key assumptions for this model are that the microcracks are penny-shaped and
721 that the rock does not undergo brittle or plastic deformation. Using the approach of Sayers &
722 Kachanov (1995) and Schoenberg & Sayers (1995), the excess compliance ΔS (the inverse
723 of the $3 \times 3 \times 3 \times 3$ elasticity tensor \mathbf{C}) due to the deformation of microcracks is used to
724 compute the stress dependence and induced elastic anisotropy

$$725 \quad \Delta S_{ijkl} = \frac{1}{4} (\delta_{ik} a_{jl} + \delta_{jk} a_{il} + \delta_{il} a_{jk} + \delta_{jl} a_{ik}),$$

726
727 where δ_{ij} is the Kronecker delta and summation convention is being used.
728

729 Appendix B: AVOA

730 The seismic reflection P-wave amplitude variation with offset and azimuth (AVOA) technique
731 was developed for detecting sub-seismic vertical fracture sets. The reflected seismic is
732 influenced by the interaction of the incident seismic wave with a discontinuity in material
733 properties (seismic velocity and/or density), where the energy of the incident wave can be
734 converted into up to six secondary waves. Although Snell's law can be used to determine the
735 directional properties of all the secondary waves, it cannot provide information on waveform
736 amplitudes and pulse distortion. Thus a more complete evaluation of the reflection and
737 transmission (R/T) properties is needed. The solution to the R/T response involves using a
738 local plane-wave and plane-boundary approximation (see Angus and Thomson 2012). The
739 AVOA technique utilises the AVOA intercept (P-wave normal-incidence reflectivity A) and two
740 gradients: an azimuthally invariant isotropic component \mathbf{G}_{iso} and an azimuthally dependent
741 anisotropic contribution \mathbf{G}_{aniso} (see Rüger 1998; Jenner 2002)

$$742 \quad R_P^{HTI}(\theta, \gamma) = A + (\mathbf{G}_{iso} + \mathbf{G}_{aniso}(\cos \gamma)^2) (\sin \theta)^2,$$

743
744 where

$$745 \quad A = \frac{1\Delta Z}{2Z}$$

746 $\mathbf{G}_{iso} = \frac{1}{2} \left[\frac{\Delta a}{a} - \left(\frac{2\beta}{a} \right)^2 \frac{\Delta G}{G} \right]$

747 $\mathbf{G}_{aniso} = \frac{1}{2} \left[\Delta\delta^{(V)} + 2 \left(\frac{2\beta}{a} \right)^2 \Delta\gamma \right]$

748

749 In Figures 6-8 we only plot the fast orientation of the anisotropy, which is orthogonal to the
750 direction of maximum \mathbf{G}_{aniso} .